

Banner appropriate to article type will appear here in typeset article

Characterisation of rough-wall drag in compressible turbulent boundary layers

D. D. Wangsawijaya^{1†}, R. Baidya^{2,3}, S. Scharnowski², B. Ganapathisubramani¹, and C. J. Kähler²

¹University of Southampton, University Road SO17 1BJ, United Kingdom

²University of the Bundeswehr Munich, Werner-Heisenberg-Weg 39, 85577 Neubiberg, Germany

³University of Melbourne, Grattan Street, Parkville VIC 3010, Australia

(Received xx; revised xx; accepted xx)

In compressible turbulent boundary layers (TBLs), roughness drag is typically characterised by first applying a velocity transformation to account for compressibility, after which the momentum deficit ΔU^+ (Hama 1954) and the equivalent sand-grain roughness k_s are inferred. In practice, k_s is often obtained from measurements at a single Mach number M and Reynolds number Re , effectively forcing the roughness into the $\Delta U^+ - \log(k_s)$ relation of Nikuradse (1933). This raises a key question: *if a rough surface has a known k_s in incompressible flow, under what conditions can this value be used in compressible flows?* This question is explored using data obtained through a series of experiments of TBLs on rough walls (P60- and P24-grit sandpapers) over $0.3 \leq M \leq 2.9$ and $7427 \leq Re_\tau \leq 30292$, including independent variation of Re_τ at $M = 2$. Results show that ΔU^+ is largely insensitive to the velocity transformation, but the fully rough regime exhibits a Mach-number-dependent shift in the logarithmic relation. Three empirical scalings are examined: an equivalent incompressible k_s , a viscosity-scaled roughness $k_* = k/\nu_\infty^+$ with $\nu_\infty^+ = \nu_\infty/\nu_w$, and a correction factor $\sqrt{1/F_c}$ where F_c depends on T_∞/T_w . The last provides the most consistent improvement across datasets, although all corrections remain empirical and rely on smooth-wall compressibility transformations. This paves the way for future work to develop custom transformation for a rough-wall TBL that can account for roughness properties and other parameters including wall conditions.

Key words:

1. Introduction

A turbulent boundary layers (TBL) developing over a rough wall is a phenomenon that may occur in both incompressible and compressible flow regimes. In the incompressible flow regime, this comprises of phenomena in the transport industry, such as biofouling on ship hulls and icing on aircraft wings, as well as geophysical flows (atmospheric boundary layers

† Email address for correspondence: D.D.Wangsawijaya@soton.ac.uk

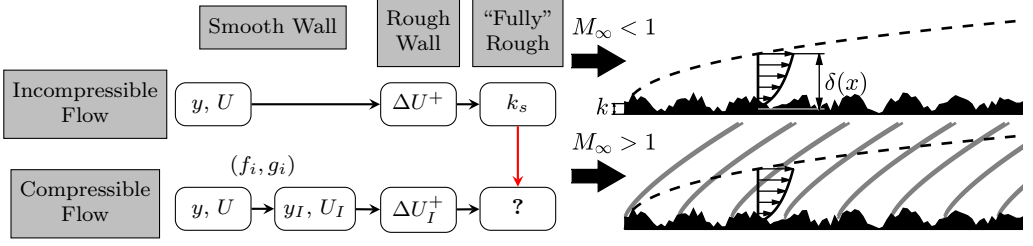


Figure 1: Established framework for drag characterisation of rough-wall turbulent boundary layers in both incompressible and compressible flow regimes.

developing over natural, urban landscapes, and water waves), to name a few examples. In the compressible flow regime, roughness (including steps and gaps) is likely to be induced by ablation, dust impact, water, ice droplets, and thermal expansion during the operation of high-speed flight vehicles.

1.1. Rough walls in incompressible flows

In the incompressible flow regime, drag penalty due to surface roughness is relatively well-defined. It is characterised by a log-law deficit from that of a smooth surface, corresponding to the Hama (1954) roughness function ΔU^+

$$U^+ = \frac{1}{\kappa} \log(y + d)^+ + B - \Delta U^+ \quad (1.1)$$

where κ is the von Kármán constant, $U^+ = U/U_\tau$ is the viscous-scaled mean streamwise velocity, $U_\tau = \sqrt{\tau_w/\rho}$ is the friction velocity, $y^+ = yU_\tau/\nu$ is the viscous-scaled wall-normal coordinates, d is the zero-plane displacement, ν is the kinematic viscosity, and B is the log-law intercept. A constant $\kappa = 0.39$ and the log-law intercept $B = 4.3$, similar to those of Squire *et al.* (2016) and Gul & Ganapathisubramani (2021), are applied to all test cases in this study.

In the so-called “fully rough” regime, where the major contribution to the total drag comes from that of the pressure drag of the test surface’s roughness elements, ΔU^+ is solely a function of the equivalent sand-grain roughness k_s (Nikuradse 1933)

$$\Delta U^+ = \frac{1}{\kappa} \log k_s^+ + B - B_{FR} \quad (1.2)$$

where $k_s^+ = k_s U_\tau/\nu$ and $B_{FR} = 8.5$ is the fully rough intercept. It should be noted that k_s is not a physical description of a roughness. Rather, it is a measure of the effect of a roughness to the flow, relative to a sand grain-type roughness. For a matched $Re_\tau = \delta U_\tau/\nu$ (δ is the boundary-layer thickness) between flows developing over a smooth and a rough walls, ΔU^+ is related to the skin friction coefficient $C_f = 2(U_\tau/U_\infty)^2$ by

$$\Delta U^+ = \sqrt{\frac{2}{C_f}} \Big|_{smooth} - \sqrt{\frac{2}{C_f}} \Big|_{rough} \quad (1.3)$$

The current framework for the drag characterisation of incompressible, rough-wall TBLs, illustrated in figure 1, is well-established: from the rough-wall U^+ obtained by flow measurements or simulations (as a function of y^+), ΔU^+ is calculated as a vertical shift from the smooth-wall logarithmic profile $1/\kappa \log(y + d)^+ + B$ (equation 1.1). If the flow falls into the fully rough regime, ΔU^+ is solely a function of k_s , which can be obtained directly from equation (1.2).

Transformation	Abbreviation	f_I	g_I
Howarth (1948)	‘HO’	$\sqrt{\frac{\rho^+}{\mu^+}}$	1
van Driest (1951)	‘VD’	1	$\sqrt{\frac{\rho^+}{\mu^+}}$
Brun <i>et al.</i> (2008)	‘BR’	$\frac{1}{\mu^+}$	$\sqrt{\frac{\rho^+}{\mu^+}} \frac{y}{y_I}$
Trettel & Larsson (2016)	‘TL’	$\frac{d}{dy} \left(\frac{y\sqrt{\rho^+}}{\mu^+} \right)$	$\mu^+ \frac{d}{dy} \left(\frac{y\sqrt{\rho^+}}{\mu^+} \right)$
Volpiani <i>et al.</i> (2020)	‘VO’	$\sqrt{\frac{\rho^+}{\mu^{+3}}}$	$\sqrt{\frac{\rho^+}{\mu^+}}$

Table 1: Various transformation functions f_I and g_I related to equation (1.4), $\rho^+ = \rho/\rho_w$ and $\mu^+ = \mu/\mu_w$ are the density and dynamic viscosity profiles as a function of wall-normal coordinates, relative to the density and dynamic viscosity at the wall.

1.2. Rough walls in compressible flows

For a wall-bounded turbulent flow developing over a *smooth* surface in the compressible flow regime, the mean velocity profile U and wall-normal coordinates y of the TBL must be transformed or “stretched” to account for the compressibility effect, such that the stretched profile U_I and coordinates y_I collapse onto the log-law of a TBL in the incompressible flow regime. In Volpiani *et al.* (2020) and Modesti *et al.* (2022), generic transformations functions f_I and g_I transform y and U into their incompressible equivalents

$$y_I = \int_0^{\hat{y}} f_I(\hat{y}) d\hat{y} \quad \text{and} \quad U_I = \int_0^{\hat{U}} g_I(\hat{U}) d\hat{U} \quad (1.4)$$

While a number of studies have been devoted to formulate various f_I and g_I , in this study we limit the analysis and discussion for 5 different transformations listed in table 1, identical to those chosen by Volpiani *et al.* (2020), and some by Modesti *et al.* (2022). These transformations are: the Van Driest I transformation (van Driest 1951, abbreviated to ‘VD’ in this study), which is the most widely known and used transformation, an older transformation (Howarth 1948, or ‘HO’), and 3 newer ones: Brun *et al.* (2008) – ‘BR’, Trettel & Larsson (2016) – ‘TL’, and Volpiani *et al.* (2020) – ‘VO’. As shown in table 1, the transformation functions f_I and g_I typically account for density and viscosity variations across the boundary-layer, $\rho^+ = \rho/\rho_w$ and $\mu^+ = \mu/\mu_w$, where $\rho = \rho(y)$ and $\mu = \mu(y)$ are the flow density and dynamic viscosity as functions of y , and the subscript ‘ w ’ denotes quantities at the wall.

For a rough surface exposed to a compressible inlet condition (figure 1, $M_\infty > 1$ is the freestream Mach number), shock waves form as the flow encounters protrusions of the roughness elements above the sonic line. Thus, in a addition to the roughness element drag in the incompressible flow regime, compressible, rough-wall TBLs generate the so-called wave drag, as illustrated in figure 1. At present, there are no f_I and g_I transformation functions that account for roughness-generated shock waves above a particular rough wall. Instead, U and y are transformed first into their incompressible equivalents, U_I and y_I via equation (1.4) and the transformation functions shown in table 1. Then, the Hama roughness function is

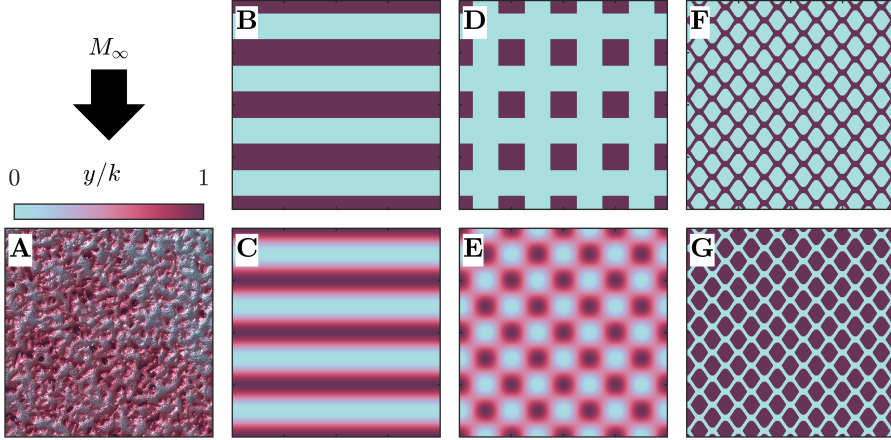


Figure 2: Coloured contours of various roughness topologies relative to the roughness element height k . Types of roughnesses from existing studies listed in table 2: type ‘A’ (sandpaper), ‘B’ (2D traverse bars), ‘C’ (2D sine waves), ‘D’ (cubes), ‘E’ (egg carton), ‘F’ (expanded mesh), and ‘G’ (diamonds). Black arrow indicates the direction of the flow.

calculated from the stretched profile U_I

$$U_I^+ = \frac{1}{\kappa} \log(y + d)_I^+ + B - \Delta U_I^+ \quad (1.5)$$

where $U_I^+ = U_I/U_\tau$, $(y + d)_I^+ = (y + d)_I U_\tau/\nu_w$, $U_\tau = \sqrt{\tau_w/\rho_w}$, and ΔU_I^+ is the Hama roughness function obtained from the transformed velocity and wall-normal coordinates. Finally, in the case of fully rough flow, the equivalent sand grain roughness k_s for a particular roughness is derived directly from its ΔU_I^+ , similar to equation 6, but with ΔU_I^+ instead of ΔU^+ .

The present drag characterisation framework for compressible, rough-wall TBLs, summarised in figure 1, is evident in the previous studies conducted on various rough surfaces at the compressible regime. The number of available studies are limited, however, we are able to categorise these studies into 7 different roughness “families”, as illustrated in figure 2: type A (sandpaper roughness), B (2D traverse bars), C (2D sine waves), D (cubes), E (egg carton roughness), F (expanded mesh), and G (diamonds).

The complete list of all previous studies on every type of roughness in figure 2 is summarised in table 2. For sandpaper roughness (figure 2A), whenever available, the grit size is reported. A wide range of roughness element sizes ($6.3 \leq \delta/k \leq 80.8$, k is the physical height of the roughness) is covered across all types of roughness shown in table 2. The majority of these studies were conducted in the supersonic flow regime, $1.5 \leq M_\infty < 5$ (or the bulk Mach number M_b in channel flow studies), with some (Sahoo *et al.* 2009; Neeb *et al.* 2024; Wang & Gao 2024) extended towards the hypersonic regime. In two studies (Tyson & Sandham 2013; Modesti *et al.* 2022), marked by ‘†’ in table 2, a baseline simulation for the same roughness was conducted in the incompressible flow regime ($M_b = 0.3$). Conditions at the wall varied: in some experimental campaigns (Sahoo *et al.* 2009; Peltier *et al.* 2016; Neeb *et al.* 2024), the wall temperatures T_w were measured directly with thermocouples or infrared thermography (marked by ‘a’ in table 2), while in another study (Reda *et al.* 1975), direct T_w measurements were only available for a reference case (typically a smooth wall), while for the rest of the roughness surfaces, adiabatic walls were assumed (‘b’ in table 2). In other studies (Goddard 1959; Berg 1979; Latin & Bowersox 2000; Ekoto *et al.* 2008), no direct

Type	Reference	$M_\infty, (M_b)$	Re_τ	δ/k	ΔU_I^+	Wall	Drag	Sym.
A	Goddard (1959)	2.75	–	59.3	2.40	Ⓒ	①	●
	Goddard (1959)	2.75	–	32.7	5.27	Ⓒ	①	●
	Goddard (1959)	2.75	–	15.3	7.95	Ⓒ	①	●
	Reda <i>et al.</i> (1975): P80	2.75	–	173	1.20	Ⓑ	①	●
	Reda <i>et al.</i> (1975): P50	2.90	–	92.6	4.50	Ⓑ	①	●
	Reda <i>et al.</i> (1975): P36	2.90	–	66.1	5.83	Ⓑ	①	●
	Reda <i>et al.</i> (1975): P24	2.90	–	40.2	7.67	Ⓑ	①	●
	Reda <i>et al.</i> (1975): P24	2.90	–	43.1	9.23	Ⓑ	①	●
	Latin & Bowersox (2000): P80	2.73	3475	27.7	8.33	Ⓒ	②	●
	Latin & Bowersox (2000): P36	2.72	5007	20.0	11.58	Ⓒ	②	●
Latin & Bowersox (2000): P20	2.70	5104	21.3	12.48	Ⓒ	②	●	
B	Berg (1979)	6.00	583	80.8	2.69	Ⓒ	①	△
	Berg (1979)	5.98	612	40.4	3.76	Ⓒ	①	△
	Berg (1979)	5.97	745	21.6	6.55	Ⓒ	①	△
	Latin & Bowersox (2000)	2.73	4454	30.0	10.82	Ⓒ	②	△
	Sahoo <i>et al.</i> (2009)	7.30	733	7.3	13.00	Ⓐ	④	▲
C	Tyson & Sandham (2013) [†]	(1.5, 3)	160, 180	12.5	4.24, 4.02	Ⓓ	③	▽
	Tyson & Sandham (2013) [†]	(1.5, 3)	160, 180	6.3	7.09, 6.70	Ⓓ	③	▽
	Aghaei-Jouybari <i>et al.</i> (2023)	(1.50)	236, 250	10.0	6.61, 7.76	Ⓓ	③	▽
D	Latin & Bowersox (2000)	2.73	4184	28.2	10.38	Ⓒ	②	■
	Ekoto <i>et al.</i> (2008)	2.86	6235	14.7	12.20	Ⓒ	④	■
	Modesti <i>et al.</i> (2022) [†]	(2, 4)	498–2688	12.5	5.04–8.83	Ⓔ	③	■
	Neeb <i>et al.</i> (2024)	4.9–5.2	307–384	8.6–11	5.62–6.34	Ⓐ	④	■
E	Aghaei-Jouybari <i>et al.</i> (2023)	(1.50)	225, 235	10.0	5.15, 6.30	Ⓓ	③	▶
	Wang & Gao (2024)	2.3–7.3	581–625	12.7–13.5	9.20	Ⓓ	③	▶
F	Sahoo <i>et al.</i> (2009)	7.30	846	6.3	13.80	Ⓐ	④	◀
G	Ekoto <i>et al.</i> (2008)	2.86	4575	13.9	–	Ⓒ	④	◆
	Peltier <i>et al.</i> (2016)	4.89	2300	14.1	13.00	Ⓐ	④	◆

Table 2: Summary of previous studies conducted on rough-wall in compressible, wall-bounded turbulence. Roughness types correspond to figure 2. M_∞ is the freestream Mach number, while M_b (in brackets) is the bulk Mach number of channel flow studies.

Column ‘Wall’ refers to various conditions at the wall, which are Ⓐ: direct wall temperature T_w measurements, Ⓑ: direct T_w measurements only for a reference case, adiabatic wall was assumed for the rest of the test cases, Ⓒ: adiabatic wall was assumed, Ⓓ: isothermal wall was set as the simulation’s boundary condition and Ⓔ: cooled wall was set as the simulation’s boundary condition. Column ‘Drag’ refers to various techniques to obtain the WSS, which are ①: direct WSS measurements, ②: direct WSS measurements only for a reference case, a fitting method utilised for the rest of the test cases, ③: WSS from the wall velocity gradient, and ④: WSS obtained from a fitting method. ‘†’ denotes available incompressible flow simulations at $M_b = 0.3$. Symbols denote various roughness types, with grey shades denoting different studies.

measurements of T_w were available and thus adiabatic walls were assumed (‘**c**’ in table 2). In numerical simulation studies, T_w was somewhat imposed as a boundary condition: either isothermal walls (Tyson & Sandham 2013; Aghaei-Jouybari *et al.* 2023; Wang & Gao 2024) or walls cooled by a certain cooling rate (Modesti *et al.* 2022). These studies are marked by ‘**d**’ and ‘**e**’ in table 2, respectively.

In terms of the wall shear stress (WSS), direct measurements using drag balance were conducted in some experimental studies (Goddard 1959; Reda *et al.* 1975; Berg 1979), marked by ‘**1**’ in table 2, or it was obtained from the velocity gradient on the wall in numerical simulations of Tyson & Sandham (2013); Modesti *et al.* (2022); Aghaei-Jouybari *et al.* (2023); Wang & Gao (2024) (‘**3**’ in table 2). Latin & Bowersox (2000) limited the direct WSS measurements to a reference smooth wall case (marked by ‘**2**’ in table 2), while the rough WSS was obtained using some profile fitting techniques, similar to those described in §2.5. When direct measurements were not supported in the experimental facilities (Ekoto *et al.* 2008; Sahoo *et al.* 2009; Peltier *et al.* 2016; Neeb *et al.* 2024), fitting techniques were used for the entirety of the experimental data. These are marked by ‘**4**’ in table 2. The obtained WSS, either from fitting or direct measurements, was then combined with the stretched U_I and y_I via equation (1.4) to determine ΔU_I^+ (figure 1). A large majority of studies in table 2 used VD transformation (formula shown in table 1), while in Modesti *et al.* (2022), other transformations such as TL and VO were used in addition to the VD transformation. A custom transformation was used by Wang & Gao (2024). From there, the vertical shift ΔU_I^+ was determined, and the reported values are listed in table 2.

1.3. Aim, scope, and limitations

As shown in table 2, all experimental studies on rough walls in compressible flows were conducted at a single M_∞ and Re_τ (which was determined by M_∞). In some simulations (Tyson & Sandham 2013; Wang & Gao 2024), M_b sweeps were conducted, while in Modesti *et al.* (2022) an independent Re_τ sweep at a constant M_b was also conducted. For the measurements conducted at a single M_∞ and Re_τ , k_s of a certain roughness was directly derived from the obtained ΔU_I^+ (figure 1), implying that this k_s is *forced* to collapse onto Nikuradse’s formula for incompressible flows (Nikuradse 1933).

Considering this existing framework (figure 1) for drag characterisation of rough walls in compressible flows, and the limited amount of data available in this flow regime (table 2) compared to those within the incompressible flow regime, we aim to investigate the possibility of transferring the established framework for rough-wall drag in incompressible flows to the compressible flow regime. This is illustrated by the red arrow in figure 1: *if k_s of a certain roughness in incompressible flows is known, what would it take to use this k_s for the same roughness in compressible flows?* We note that this approach is not new; a similar approach has been attempted by Modesti *et al.* (2022) for direct numerical simulations of a channel flow covered with cube roughness (figure 2D), where k_s from a simulation at $M_b = 0.3$ must be corrected by a factor for drag characterisation at $M_b = 2$ and 4. Therefore, in this study, we intend to fill in the remaining gaps with experimental data in a higher range of Re_τ ($7427 \leq Re_\tau \leq 30292$) for two types of realistic, sandpaper-like surface roughness (figure 2A). A range of nominal test section Mach numbers M is covered in this study, spanning subsonic ($M = 0.3$), transonic ($M = 0.8$), and supersonic flow regimes (up to $M = 2.9$), completed with an independent variation of Re_τ at a constant $M = 2$, as detailed in §2. In §4, the new framework (figure 1) will be tested for various compressibility transformations shown in table 1, as well as data from previous studies in table 2, and the results will be discussed further in §5. We acknowledge that, while the experimental facility enables independent Re and M sweeps, its limitations prevent direct T_w

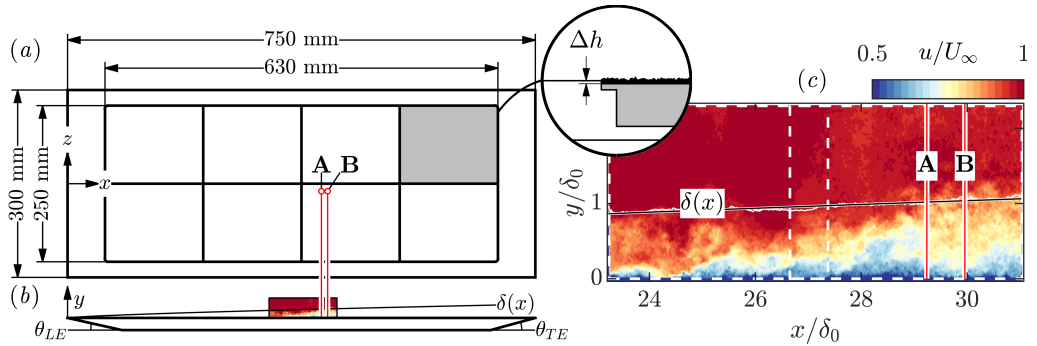


Figure 3: (a) Top view (x - z plane) and (b) side view (x - y plane) of the baseplate with 8 inserts where the rough surfaces are attached. Red circles and solid lines mark ‘A’ and ‘B’ measurement stations. Black solid lines mark the 99% boundary-layer thickness growth $\delta(x)$, while θ_{LE} and θ_{TE} are the leading and trailing edge ramp angles relative to the x -direction. *Inset*: cross-sectional view of the baseplate with an insert (gray-shaded), showing the insert’s thickness lowered by Δh to approximately match the height of the baseplate and the rough walls (black-shaded). (c) Coloured contours of the normalised instantaneous streamwise velocity u/U_∞ of the reference case (SW at $M = 0.3$). White solid line shows the $\delta(x)$ obtained from PIV measurements. Black solid line marks the power law fit $0.194x^{0.714}$ (in mm), obtained by fitting $\delta(x)$ of the reference case. White dashed lines mark the FOVs from the two PIV cameras, with 10 mm overlap in x -direction. δ_0 is the δ averaged over $x = 407 \pm 5$ mm (station ‘A’).

and WSS measurements on the rough walls. The estimation techniques for these quantities are detailed in §2.4 and §2.5, respectively.

2. Methodology

2.1. Facility and air properties

Measurements are conducted inside the intermittent, blow-down trisonic wind tunnel (TWM) facility at the University of the Bundeswehr Munich. Compressed air is pumped into the holding tanks prior to each experimental run, released into the $1800 \text{ mm} \times 300 \text{ mm} \times 675 \text{ mm}$ (length \times width \times height) test section, and finally exhausted to the atmosphere. The facility is equipped with an adjustable Laval nozzle and a diffuser, allowing a range of operating Mach numbers of $0.3 \leq M \leq 3$. Within this operational range, the freestream turbulence intensity ranges from 1.9% to 4.5% (inversely proportional to M), as recorded by Scharnowski *et al.* (2019).

Table 3 shows key air properties of all test cases. For all test cases, the experimental data are recorded for approximately 20 s for each run. The mean stagnation pressure P_0 (subscript ‘0’ denotes a total or stagnation quantity) is recorded in the settling chamber, while the mean stagnation temperature T_0 is measured in the holding tanks. The mean nominal test section Mach number M is obtained from the isentropic relation, while M_∞ and U_∞ are the mean freestream Mach number and velocity obtained from PIV measurements at the measurement stations shown in figure 3(a). For the viscous-scaled quantities shown in table 3, the dynamic viscosity μ is calculated using Sutherland’s formula. The complete description of the test facility is given by Baidya *et al.* (2020).

2.2. Test cases

Measurements are conducted for the TBLs developing over a $750 \text{ mm} \times 300 \text{ mm} \times 19.5 \text{ mm}$ ($58\delta_0 \times 22\delta_0 \times 1.4\delta_0$, length \times width \times maximum height) smooth baseplate (figure

M	M_∞	P_0	T_0	T_∞/T_w	U_∞	$U_{\tau VD}$	δ	θ	$Re_{\tau VD}$	C_{fVD}	ΔU_{VD}^+	Symbol				
[-]	[-]	[bar]	[K]	[-]	[m/s]	[m/s]	[mm]	[mm]	[-]	$[\times 10^{-3}]$	[-]	HO	VD	BR	TL	VO
Smooth Wall (SW)																
0.3	0.28	1.5	293	0.99	93.82	3.36	13.92	1.38	4355	2.53	-	○	△	□	◇	☆
0.8	0.80	1.5	286	0.90	255.45	8.76	22.29	1.86	13361	2.11	-	○	△	□	◇	☆
2.0	1.90	2.5	287	0.61	492.62	18.63	8.15	0.87	4140	1.73	-	○	△	□	◇	☆
2.0	1.90	4.5	285	0.61	491.16	17.86	7.85	0.78	6933	1.60	-	○	△	□	◇	☆
2.9	2.89	4.5	289	0.40	602.71	26.11	7.81	0.75	2233	1.50	-	○	△	□	◇	☆
Rough Wall (P60)																
0.3	0.29	1.5	296	0.99	97.66	4.89	16.57	1.99	7427	4.95	9.84	○	△	□	◇	☆
0.8	0.82	1.5	289	0.89	261.93	13.82	24.44	2.56	22391	4.97	11.80	○	△	□	◇	☆
2.0	1.95	2.5	284	0.60	496.40	34.70	11.61	1.50	10446	5.82	13.96	○	△	□	◇	☆
2.0	1.91	4.5	286	0.61	492.10	34.60	11.92	1.52	20271	5.99	15.33	○	△	□	◇	☆
2.9	2.84	4.5	291	0.41	601.55	62.89	10.75	1.32	7812	8.93	16.41	○	△	□	◇	☆
Rough Wall (P24)																
0.3	0.28	1.5	295	0.99	97.02	5.67	18.83	2.53	9830	6.74	13.29	○	△	□	◇	☆
0.8	0.80	1.5	287	0.90	255.33	16.42	24.17	2.96	27025	7.42	15.86	○	△	□	◇	☆
2.0	1.99	2.5	279	0.59	497.41	41.40	14.90	2.03	15594	8.11	17.09	○	△	□	◇	☆
2.0	1.94	4.5	286	0.60	496.18	42.76	15.05	2.03	30292	8.89	19.22	○	△	□	◇	☆
2.9	2.77	4.5	292	0.42	596.43	67.65	12.92	1.64	11167	10.82	18.61	○	△	□	◇	☆

Table 3: Summary of all test cases. The air properties are: M (nominal test section Mach number), M_∞ (freestream Mach number obtained from PIV measurements at the measurement stations in figure 3c), stagnation pressure and temperature (P_0 and T_0). T_∞/T_w is the freestream-to-wall temperature ratio. The 99% boundary-layer thickness δ and momentum thickness θ are obtained from untransformed velocity profiles extracted either from measurement station **A** or **B** in figure 3(c). The friction velocity U_τ and other related quantities (Re_τ , C_f , and ΔU_τ^+) are estimated using methods described in §2.5 all transformations in table 1. For brevity, only results from van Driest (1951) transformation are shown here. Symbols denote various transformations (table 1), with lighter to darker colour schemes mark the lowest to highest Mach numbers.

3a) suspended at the test section half-height, where δ_0 is the reference 99% smooth-wall boundary-layer thickness at $M = 0.3$. Flow measurements are conducted on the TBL developing over the flat surface of the baseplate, while the bottom surface has the wedge angles of $\theta_{LE} = 12.6^\circ$ and $\theta_{TE} = 15.2^\circ$ at the leading and trailing edges, respectively, as illustrated in figure 3(b). Eight removable inserts, each has the dimensions of $157.5 \text{ mm} \times 125 \text{ mm}$, are arranged in a manner shown in figure 3(a), allowing multiple changes of test surfaces without removing the base plate from the test section. With this configuration, the rough test surfaces only cover an area of $630 \text{ mm} \times 250 \text{ mm}$ ($42\delta_0 \times 18\delta_0$) of the baseplate, while the edges of the baseplate are smooth (figure 3a).

Test surfaces comprise of a smooth wall (case ‘SW’) and two rough walls constructed from

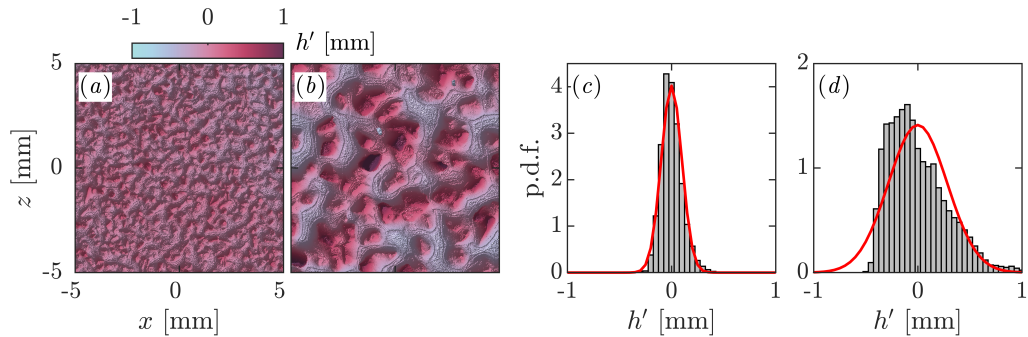


Figure 4: Coloured contours of the scanned sandpaper surface deviation from its mean height, $h' = h - \bar{h}$, shown for 10 mm \times 10 mm coupons of (a) P60- and (b) P24-grit sandpapers. Probability density function (p.d.f.) of h' of the scanned (c) P60- and (d) P24-grit sandpapers. Solid red line (—) is the fitted Gaussian distribution of the p.d.f.

Parameter:	k	k_a	k_p	k_{rms}	k_{sk}	k_{ku}	ES_x
Formula:	$6\sqrt{h'^2}$	$ \overline{h'} $	$\max(h') - \min(h')$	$\sqrt{h'^2}$	$\overline{h'^3}/h_{rms}^3$	$\overline{h'^4}/h_{rms}^4$	$ \frac{dh'}{dx} $
Unit:	mm	mm	mm	mm	—	—	—
P60	0.595	0.077	0.804	0.099	1.261	10.375	0.541
P24	1.695	0.226	2.023	0.283	1.841	9.708	0.659

Table 4: Key surface parameters from the scanned P60- and P24-grit sandpaper coupons.

P60- and P24-grit sandpaper sheets (cases ‘P60’ and ‘P24’, respectively). Surface topologies are obtained from samples of P60 and P24 sandpapers prior to the measurement campaigns. A 10 mm \times 10 mm coupon of P60 and a 13 mm \times 13 mm coupon of P24 sandpapers are scanned using an Alicona G4 InfiniteFocus optical profilometer. The topologies are shown as the scanned surface deviations from their mean heights ($h' = h - \bar{h}$) in figures 4(a,b), while their roughness height distributions are shown in figures 4(c,d). The physical height of the roughness is defined by $k = 6\sqrt{h'^2}$, yielding $k = 0.595$ mm for P60 and $k = 1.695$ mm for P24 sandpapers, respectively. This parameter, alongside other key surface parameters similar to those of Squire *et al.* (2016) and Gul & Ganapathisubramani (2021), are presented in table 4. The sandpaper sheets are cut to the size of the baseplate inserts (figure 3a) and attached to the inserts using double-sided carpet tapes. Since the flow encounters two step changes in roughness as the TBL develops: first the smooth leading edge to the rough surface inserts, followed by the smooth trailing edge of the baseplate, extra care is taken to minimise the height difference between the smooth baseplate and the rough surfaces by lowering the insert’s thickness by $\Delta h = 1$ mm and 1.5 mm for P60 and P24 surfaces, respectively (see inset in figure 3a). The required Δh values are determined by taking the side images of the P60 and P24 sandpaper coupons (with their base papers and double-sided tapes) against a metal shim of known thickness.

For analyses in this study, velocity profiles are extracted from and averaged over $x = 407 \pm 5$ mm ($x/\delta_0 \approx 29 \pm 0.36$) from the leading edge of the baseplate for SW and P24 cases

(station ‘A’ in figure 3a) to improve statistical convergence. Due to wall reflections issue in the PIV images, the profiles of P60 cases are instead extracted from and averaged over station ‘B’, $x = 417 \pm 5$ mm ($x/\delta_0 \approx 30 \pm 0.36$, figure 3a). Table 3 shows the complete test matrix and the corresponding test parameters measured at these stations. For brevity, only friction velocity U_τ , the Hama roughness function ΔU_I^+ , and subsequently the friction Reynolds number $Re_\tau = \delta U_\tau/\nu_w$ and the skin friction coefficient,

$$C_f = 2 \frac{\rho_w}{\rho_\infty} \left(\frac{U_\tau}{U_\infty} \right)^2 \quad (2.1)$$

estimated from the profiles stretched by VD transformation are shown in table 3, denoted by subscript ‘VD’. Note that, here, U_∞ refers to the actual freestream velocity, without any transformation. All test surfaces are subjected to a range of Mach numbers ($0.3 \leq M \leq 2.9$) and friction Reynolds numbers ($4355 \leq Re_{\tau_{VD}} = \delta U_{\tau_{VD}}/\nu_w \leq 30292$). At a constant Mach number ($M = 2$), the stagnation pressure of the tunnel P_0 is varied from 2.5 to 4.5 bar (table 3), allowing an independent sweep of Re_τ while maintaining a constant M .

2.3. PIV measurements

Non-time-resolved planar 2D2C particle image velocimetry (PIV) measurements are conducted on the streamwise–wall-normal (x – y) plane, shown in figure 3(b,c), located at $z = 12$ mm from the centreline of the tunnel (figure 3a). The measurement plane is illuminated by a laser sheet generated by an InnoLas SpitLight Compact PIV 400 dual-pulse Nd:YAG laser with a typical optical configuration. The flow is seeded with DEHS (Di-Ethyl-Hexyl-Sebacat) tracer particles, whose mean diameter is approximately 1 μm (Kähler *et al.* 2002). As many as 400 image pairs are captured for each test case shown in table 3 by two 16-bit, 5.5 MP LaVision Imager sCMOS CLHS cameras (2560×2160 pixels sensor resolution), each equipped with a Zeiss Milvus 100mm f/2.0 lens. White dashed lines in figure 3(c) mark the FOV (field-of-view) captured by each camera, with 10-mm overlap between the cameras. Stitched together, the camera arrangement yields a FOV spanning 109 mm in length and 32 mm in height ($7.8\delta_0 \times 2.3\delta_0$).

For all test cases in table 3, PIV images are acquired at a constant rate of $f = 10.5$ Hz. The time between images Δt is set to be inversely proportional to the nominal test section Mach numbers, between 0.65 to 4 μs for test cases $M = 2.9$ to $M = 0.3$, respectively. For the reference test case (SW at $M = 0.3$), this acquisition setup corresponds to the viscous-scaled sampling interval of $t^+ \equiv \Delta t U_\tau^2/\nu_w = 2.8$ and the boundary-layer turnover rate of $U_\infty/(f\delta_0) = 723$.

PIV calibration is conducted prior to the measurements. The current setup yields an image pixel size of 27–28 $\mu\text{m}/\text{pixel}$ between the two cameras. PIV cross-correlation is performed using an in-house PIV package developed at the University of Southampton (Lawson 2016). The final correlation window size is 16×16 pixels (50% overlap), corresponding to a viscous-scaled spatial resolution of $\Delta x^+ = \Delta y^+ = 134$ for the reference test case. The uncertainties of the PIV measurements are estimated using the nominal subpixel uncertainty of 0.1 pixels (Adrian & Westerweel 2011), yielding the uncertainties of $\pm 0.6\%$ and $\pm 3.8\%$ of the maximum pixel displacements for u and v velocity components, respectively ($\pm 1.2\%$ and $\pm 7.6\%$ for their variances).

2.4. Temperature profiles

Due to limitations of the test facility, the mean wall temperature T_w and the mean temperature profile across the boundary layer $T(y)$ are not measured during the experimental campaign. Thus, these quantities are estimated based on similar experiments on rough-wall

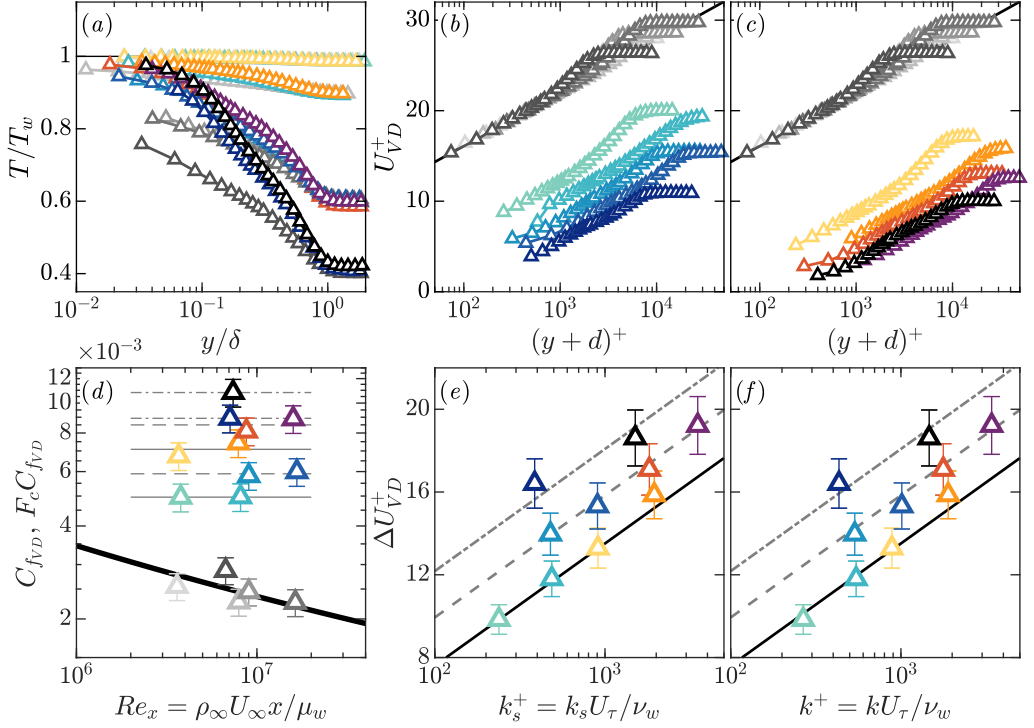


Figure 5: (a) Mean temperature profile T/T_w as function of y/δ (colours correspond to various test surfaces and M sweep shown in table 3). Inner-scaled mean streamwise velocity profile for cases (b) SW and P60, (c) SW and P24 stretched by VD transformation (table 1). —: $1/\kappa \log y^+ + B$. (d) Skin friction coefficients C_f vs Re_x estimated from VD-transformed profiles. SW data are multiplied by F_c (equation 3.1), —: $[2 \log_{10} Re_x - 0.65]^{-7/3}$ (Schlichting & Gersten 1960). Lines correspond to constant C_f , —: $M < 1$, - - - : $M = 2$, and - · - · - : $M = 2.9$. ΔU_{VD}^+ as a function of (e) k_s^+ and (f) k^+ for all rough-wall cases. Error bars in (d–f) denote the uncertainties estimated in §3. Lines correspond to log-relation, —: $M < 1$, $1/\kappa \log k_s^+ + B - B_{FR}$, - - - : $M = 2$, and - · - · - : $M = 2.9$. Colours corresponds to the test surfaces, M and Re sweeps (table 3).

TBLs conducted in similar test facilities (intermittent, blow-down supersonic wind tunnels). In Goddard (1959); Latin & Bowersox (2000); Ekoto *et al.* (2008), for example, it was assumed that zero-pressure gradient, rough-wall TBLs develop over adiabatic walls.

Using the same assumption, T_w is equal to the adiabatic wall temperature T_{aw} and the temperature-velocity profile has a quadratic relation to the mean streamwise velocity profile (Crocco 1948; Walz 1959) given by,

$$T_w = T_{aw} = T_\infty \left(1 + r \frac{\gamma - 1}{2} M_\infty^2 \right) \quad (2.2)$$

$$\frac{T}{T_\infty} = 1 + r \frac{\gamma - 1}{2} M_\infty^2 \left[1 - \left(\frac{U}{U_\infty} \right)^2 \right] \quad (2.3)$$

where the recovery factor $r = Pr^{1/3}$ and $Pr = 0.72$ is the Prandtl number (Pirozzoli & Bernardini 2011). The mean temperature profiles relative to the wall temperature T/T_w of all test cases are shown in figure 5(a) as a function of wall-normal locations y/δ (note that y shown in this figure is corrected using techniques described in §2.5). At the wall, $T/T_w = 1$

(solid black line in figure 5a), and it decreases towards the freestream following the quadratic relation in equation (2.3). The freestream-to-wall temperature ratios T_∞/T_w for all test cases are listed in table 3, showing that the temperature profile proportionally decreases with M . At the lowest Mach number ($M = 0.3$), the compressibility effect is largely negligible as T_∞ is 1% lower than T_w ($T_\infty/T_w = 0.99$). As M increases to the transonic flow regime, $T_\infty/T_w \approx 0.90$ and finally, in the supersonic regime, it decreases further to $T_\infty/T_w \approx 0.60$ and 0.40 at $M = 2$ and 2.9, respectively.

To account for the compressibility effect, the transformation functions f_I and g_I listed in table 1 require the density and viscosity profiles relative to the wall, ρ^+ and μ^+ , to be known. These quantities are derived from the temperature profiles T^+ , from the boundary layer equation $\partial P/\partial y = 0$ and Sutherland's formula,

$$\rho^+ = \frac{\rho}{\rho_w} = \left(\frac{T}{T_w}\right)^{-1} \quad \text{and} \quad \mu^+ = \frac{\mu}{\mu_w} = \left(\frac{T}{T_w}\right)^{1.5} \left(\frac{T_w + S}{T + S}\right) \quad (2.4)$$

where $S = 110.4$ K.

2.5. Wall position correction and shear stress estimation

Similar to the temperature profiles and wall temperatures, the wall shear stress (WSS) is not directly measured in the experiment. For all test cases in table 3, a modified Clauser (1954) fitting is employed. This method requires some correction of the wall-normal coordinates alongside the friction velocity U_τ estimation. Thus, to minimise uncertainty, another technique is applied to determine the wall location *before* estimating U_τ with Clauser fitting.

For SW test cases, the wall-normal grid position y is first corrected based on the location of the light-sheet reflection on the wall in the PIV images. Then, the Clauser method searches for a set of parameters (U_τ, ε) , where ε is a further wall correction of a much smaller order ($O(0.1$ mm)) than the first wall correction determined using PIV images, that minimises the r.m.s. (root mean square) error of

$$\Psi_{smooth} = U_I^+ - \left[\frac{1}{\kappa} \log \left(\frac{(y + \varepsilon)_I U_\tau}{\nu_w} \right) + B \right] \quad (2.5)$$

in the log region $30 \leq (y + \varepsilon)_I^+ \leq 0.15 Re_{\tau_I}$, where $Re_{\tau_I} = \delta_I U_\tau / \nu_w$ and δ_I is the boundary-layer thickness of the transformed velocity profile.

For P60 and P24 cases, two parameters are added to the set: the zero plane displacement d and the transformed Hama roughness function ΔU_I^+ (equation 1.1). Similar to the approach by Squire *et al.* (2016); Gul & Ganapathisubramani (2021) for sandpaper roughness, as well as Modesti *et al.* (2022) for cube roughness (figure 2D), d is kept constant at $d = -k/2$, where the physical roughness height k is determined through surface scanning (table 4). The sandpaper grain reflection on the PIV images is then used to determine the wall location and its downward shift by $k/2$ for the rough wall cases. The final parameter set is $(U_\tau, \varepsilon, \Delta U_I^+)$ that minimise the r.m.s. error of

$$\Psi_{rough} = U_I^+ - \left[\frac{1}{\kappa} \log \left(\frac{(y - k/2 + \varepsilon)_I U_\tau}{\nu_w} \right) + B - \Delta U_I^+ \right] \quad (2.6)$$

within the inertial range $3\sqrt{Re_{\tau_I}} \leq (y - k/2 + \varepsilon)_I^+ \leq 0.15 Re_{\tau_I}$ (Squire *et al.* 2016; Gul & Ganapathisubramani 2021). To further minimise the uncertainty for rough wall cases, ε is only fitted for profiles stretched by the VD transformation, where $y = y_I$ (table 1). This wall correction ε_{VD} is then applied to the profiles before stretching them with other transformations listed in table 1, and the wall location y is not corrected further in the Clauser fitting.

3. Mean flow and rough-wall skin friction

The inner-scaled transformed mean streamwise velocity $U_I^+ = U_I/U_\tau$ profiles for the P60 and P24 rough-wall cases are shown in figure 5(b,c), respectively, as a function of the inner-scaled transformed wall-normal coordinates $(y+d)_I^+ = (y+d)_I U_\tau/\nu_w$. For brevity, here we will only discuss the VD-transformed profiles, U_{VD}^+ , and sensitivity to using a different transformation will be discussed in the following section. Gray colour schemes denote SW cases (table 3), showing the transformed profiles collapsing onto the log relation $1/\kappa \log y^+ + B$, as prescribed by the modified Clauser fitting in §2.5. In contrast, the rough wall cases show a clear downward vertical shift by ΔU_{VD}^+ , obtained from §2.5.

From the fitted U_τ , the skin friction coefficient C_f is calculated using equation (2.1). Figure 5(d) shows C_f as a function of Reynolds number based on the fetch lengths Re_x for all test cases. The uncertainties of C_f are estimated via the propagation of uncertainty analysis of equation (2.1). Here, we assume the expected U_τ error range of $\pm 5\%$ for the current estimation method in §2.5 (Squire *et al.* 2016). Other variable, ρ_w/ρ_∞ , is a function of M_∞ via equations (2.4) and (2.3). The uncertainty of U_∞ is estimated via the uncertainty of the maximum pixel displacement in x of $\pm 0.6\%$ (outlined in §2.3). The propagation of uncertainty analysis yields the C_f estimation error of $\pm 10.28\%$, denoted by the error bars in figure 5(d). The black solid line denotes Schlichting's fit for incompressible, smooth-wall TBLs, $C_f = [2 \log_{10} Re_x - 0.65]^{-7/3}$ (Schlichting & Gersten 1960). To match the incompressible smooth-wall C_f , Hopkins & Inouye (1971) derived a correction factor F_c from the VD II transformation (van Driest 1956) for adiabatic walls,

$$F_c = \frac{T_w/T_\infty - 1}{\arcsin^2 \alpha}, \quad \text{where} \quad \alpha = \frac{T_w/T_\infty - 1}{\sqrt{T_w/T_\infty(T_w/T_\infty - 1)}} \quad (3.1)$$

such that the corrected skin friction of a compressible smooth wall $F_c C_f$ is equivalent to that of the incompressible flow. It is noted that F_c defined in equation (3.1) is also equal to $(\rho_\infty/\rho_w)(U_\infty/U_{\infty VD})^2$, where $U_{\infty VD}$ is the freestream velocity of the VD-transformed velocity profile. Meanwhile, the Reynolds number is corrected by a factor of μ_∞/μ_w (Hopkins & Inouye 1971), which results in the definition of $Re_x = \rho_\infty U_\infty x/\mu_w$ as the x -axis of figure 5(d). Grey coloured symbols in figure 5(d) are $F_c C_f$ as a function of Re_x for SW cases, showing that the estimated (in §2.5) and corrected C_f across M and Re sweeps largely match Schlichting's fit for incompressible, smooth-wall TBLs.

To the best of the authors' knowledge, no correction factor exists for C_f of compressible, rough-wall TBLs. Therefore, the estimated C_f for P60 and P24 cases in figure 5(d) are presented without any correction factor, following Goddard (1959). For all rough-wall cases, the fitted $\Delta U_I^+ > 7$, and thus these cases are within the fully rough regime. This is evident in the subsonic to transonic cases ($M = 0.3$ and 0.8): C_f is independent of Re_x for the same sandpaper roughness and the data largely collapse to the grey solid lines in figure 5(d). As the flow reaches the supersonic regime, it appears that there is an additional dependency on M . For the same roughness (either P60 or P24), $M = 2$ and 2.9 cases suggest a higher C_f from that of subsonic and transonic cases, which increases proportionally with M (grey dashed and dash-dot lines in figure 5d). At $M = 2$, where Re sweep is available (table 3), C_f appears to be independent of Re_x , as suggested by the estimated C_f data collapsing onto grey dashed lines in figure 5(d). Figures 5(e,f) show the fitted Hama roughness functions from the stretched velocity profiles ΔU_I^+ (in §2.5) for all P60 and P24 cases (table 3). The error bars in figures 5(e,f) show the uncertainties of $\Delta U_{VD}^+ \pm 7.3\%$ for all test cases listed in table 3, based on propagating the C_f uncertainties via equation (1.3).

Since we are looking to transform the established framework for incompressible, rough-wall TBLs to the compressible one (figure 1), k_s is determined solely from the fitted ΔU_{VD}^+

for the incompressible cases at $M = 0.3$. The P60 and P24 cases at $M = 0.3$ are within the fully rough regime, and thus the incompressible k_s can be derived directly from equation (1.2), yielding $k_s = 0.531$ and 1.742 mm for P60 and P24 cases, respectively. In figure 5(e), ' k_s ' refers to these values.

Using the above incompressible k_s , the fitted ΔU_{VD}^+ for all P60 and P24 cases in table 3 is shown in figure 5(e) as a function of $k_s^+ = k_s U_\tau / \nu_w$. Results suggest that all cases are within the fully rough regime ($\Delta U_{VD}^+ > 7$ or $k_s^+ > 70$). The collapse of $M = 0.3$ data to the log relation (equation (1.2), black solid line in figure 5e) is given since the incompressible k_s is derived from this relation. However, the collapse is also observed for the transonic ($M = 0.8$) cases. As M reaches the supersonic regime, there seems to be a proportional relation between M and the log-law intercept: the intercept $B - B_{FR}$ (equation 1.2) increases with M for the supersonic cases (grey dashed line for $M = 2$ and grey dash-dot line for $M = 2.9$ in figure 5e), possibly related to the wave drag generated by protrusion of the roughness elements. These observations still hold if the fitted ΔU_{VD}^+ is shown as a function of the inner-scaled physical roughness height $k^+ = k U_\tau / \nu_w$ instead of k_s^+ , as shown in figure 5(f).

4. Correction factors

Figure 6(a) summarises the estimated Hama roughness function ΔU_I^+ for the test cases in table 3 and previous studies (in gray filled symbols) listed in table 2 for various roughness families in figure 2. Various open symbols in figure 6(a) correspond to the fitted ΔU_I^+ of the present test cases in table 3, obtained from velocity profiles stretched by various transformations listed in table 1. For the current experimental data, the fitted ΔU_I^+ is relatively independent of transformations to account for compressibility effects. The same phenomenon observed for ΔU_{VD}^+ in figure 5(f) is still apparent if different transformations are used to obtain ΔU_I^+ : the collapse of subsonic data ($M \leq 0.8$) to Nikuradse's formula for incompressible flows (equation 1.2) and the subsequent upward shift of the log-law intercept that seems to be proportional to M at supersonic regime (gray dashed and dash-dot lines in figure 6a).

As in the current study, previous studies estimated ΔU_I^+ by fitting the downward shift of the transformed velocity profiles. The friction drag was either obtained from numerical simulations, directly measured, or, when direct measurement was not possible in the facilities, a fitting method (similar to that described in §2.5), as outlined in §1. In terms of k_s , it is worth noting that: (i) the collapse to the log-relation in equation (1.2) is forced since k_s was derived directly from the estimated ΔU_I^+ for a given M and Re in the majority of the previous studies, (ii) k_s was not reported in some studies (Goddard 1959; Reda *et al.* 1975; Sahoo *et al.* 2009; Tyson & Sandham 2013; Aghaei-Jouybari *et al.* 2023; Wang & Gao 2024), and (iii) the present experimental data (figures 5e,f) show that there is only a slight difference between using the incompressible k_s or the physical roughness height k to scale ΔU_I^+ . Considering these factors, figure 6(a) scales the x -axis with k instead of k_s , and the subsequent analyses in this study utilise k instead of the reported k_s .

Observing previous studies' data in figure 6(a), it is apparent that the majority of the test cases do not collapse to Nikuradse's data (Nikuradse 1933) for either hydrodynamically smooth ($k_s^+ < 5$), transitionally ($5 \leq k_s^+ \leq 70$), or fully rough surfaces ($k_s^+ > 70$). To be consistent with present data, we use $\kappa = 0.39$, $B = 4.3$, and $B_{FR} = 8.5$. There appears to be a tendency towards an upward shift in the intercept $B - B_{FR}$, similar to that observed in the current study. Although the shift is likely caused by the x -axis scaling by k^+ instead of k_s^+ , a collapse to Nikuradse's data is observed for some sandpaper roughness cases (Goddard 1959; Reda *et al.* 1975; Latin & Bowersox 2000) and some cube roughness cases (Modesti *et al.* 2022). Whether this upward shift is proportional to M , as suggested by the current experimental data, is even more difficult to say as the test cases in the previous studies covered

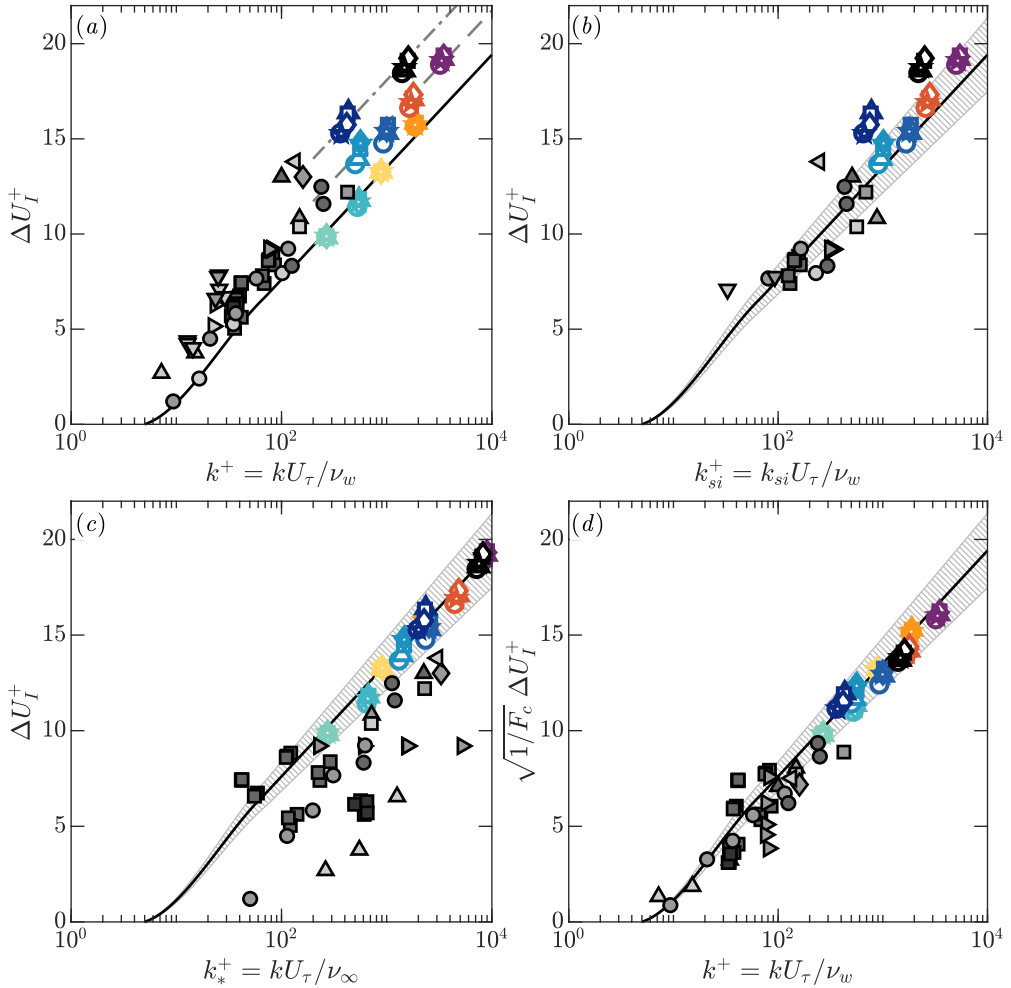
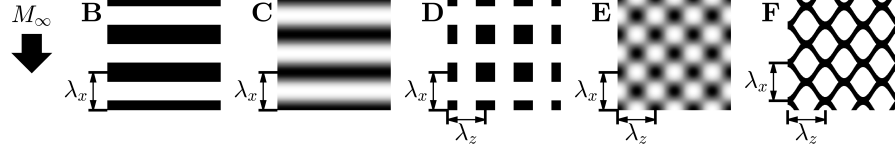


Figure 6: Hama roughness function (obtained from transformed velocity profiles) ΔU_I^+ of all test cases in table 3 and previous studies in table 2 as a function of: (a) $k^+ = kU_\tau/\nu_w$, (b) $k_{si}^+ = k_{si}U_\tau/\nu_w$ (k_{si} is obtained from matched studies in incompressible flow regime, as outlined in §4.1), and (c) $k_*^+ = kU_\tau/\nu_\infty$. In (d), ΔU_I^+ is multiplied by $\sqrt{1/F_c}$ (see equation 3.1 for the definition of F_c). —: Nikuradse's data (Nikuradse 1933), with $\kappa = 0.39$, $B = 4.3$, and $B_{FR} = 8.5$. In (a), the intercept $B - B_{FR}$ are shown by - - - : $M = 2$, and - · - · : $M = 2.9$. In (b–d), hatched regions mark the $\pm 10\%$ error from Nikuradse's data. Open coloured symbols correspond to test cases in table 3, while gray-filled symbols correspond to the previous studies in table 2.

7 different roughness families (figure 2), each with variations of their roughness parameters, with the majority of studies conducted at a single M and Re .

Taking the current and previous studies' data together, it is also apparent that in order to utilise the incompressible flow framework for drag estimation in the compressible flow regime (figure 1), either k (or k_s), i.e. the x -axis in figure 6(a), or the ΔU_I^+ (the y -axis in the same figure) must be scaled by a factor to account for the wave drag effect. Two possible scaling factors will be explored and discussed in this section.



Type	Compressible flow ($M > 1$)	δ/k	λ_x/δ	λ_z/δ	Re_τ	ΔU_I^+	Incompressible flow ($M \approx 0$)	δ/k	λ_x/δ	λ_z/δ	Re_τ	ΔU^+	k_s/k
A	Present study, P60	≈ 19	–	–	≈ 12843	≈ 15	Flack <i>et al.</i> (2007)	21	–	–	4140	10.8	1.80
	Present study, P24	≈ 8.4	–	–	≈ 19017	≈ 18	Castro (2007) [†]	9.6	0.21	0.21	3867	12.2	1.56
	Goddard (1959)	15.3	–	–	–	7.9	Flack <i>et al.</i> (2007)	16	–	–	6060	13	2.26
	Reda <i>et al.</i> (1975)	40.2	–	–	–	7.7	Gul & Ganapathisubramani (2021)	41.9	–	–	2275	6.9	1.40
	Reda <i>et al.</i> (1975)	43.1	–	–	–	9.2	Gul & Ganapathisubramani (2021)	44.2	–	–	3276	7.8	1.42
	Latin & Bowersox (2000)	27.7	–	–	3474	8.3	Brzek <i>et al.</i> (2007)	25	–	–	3789	9.7	2.36
	Latin & Bowersox (2000)	≈ 20	–	–	≈ 5056	≈ 12	Flack <i>et al.</i> (2007)	21	–	–	4140	10.8	1.80
B	Latin & Bowersox (2000)	30	0.13	–	4454	10.8	Krogstad <i>et al.</i> (2005)	29.4	0.27	–	600	8.7	5.93
	Sahoo <i>et al.</i> (2009)	7.3	0.68	–	733	13	Leonardi <i>et al.</i> (2003)	5	1	–	460	11.7	5.09
C	Tyson & Sandham (2013)	6.3	2	–	160	7.1	Tyson & Sandham (2013)	6.3	2	–	160	7.8	1.28
	Aghaei-Jouybari <i>et al.</i> (2023)	10	2	–	250	7.8	Hudson <i>et al.</i> (1996)	10	2	–	306	8.1	3.72
D	Latin & Bowersox (2000)	28.2	0.14	0.14	4184	10.4	Volino <i>et al.</i> (2011)	27.8	0.29	0.07	1869	10	1.62
	Ekoto <i>et al.</i> (2008)	14.7	0.27	0.27	6235	12.2	Castro (2007)	17.6	0.11	0.11	3278	10.4	3.80
	Modesti <i>et al.</i> (2022)	12.5	0.24	0.24	≈ 1895	≈ 8.3	Modesti <i>et al.</i> (2022)	12.5	0.24	0.24	513	7.8	1.90
E	Wang & Gao (2024)	≈ 13	0.45	0.45	608	9.2	Chan <i>et al.</i> (2015)	14	0.51	0.51	540	9.5	4.10
F	Sahoo <i>et al.</i> (2009)	6.3	0.28	0.73	845	13.8	Castro (2007)	9.8	0.33	0.97	978	9.2	1.84

Table 5: Summary of matched incompressible and compressible rough-wall TBL cases. †: matched roughness type not found.

4.1. Defining equivalent incompressible test cases

In this section, we are taking the first steps of transferring the existing framework for drag characterisation in incompressible flows for compressible flows (figure 1). Since most of the studies listed in table 2 were conducted only in the compressible flow regime, “incompressible equivalent” test cases for these studies must first be defined. Following this, an attempt is made to match the current test cases (table 3) and all the cases from previous studies (table 2) with their incompressible equivalents. Assuming that the drag (and the additional wave drag in the case of compressible flows) are proportional to the size of the physical roughness, each compressible ($M_\infty > 1$ or $M_b > 1$) case in table 3 and table 2 is matched with a previous study of the same roughness family (figure 2) and the closest available δ/k in the incompressible flow regime ($M \approx 0$). Here, we have chosen to match δ/k rather than k , since the roughness elements considered here occupy a significant portion of the log layer (i.e. $\delta/k < 40$), and therefore the equivalent sand grain roughness that fulfills equation (1.2) is expected show a dependency on k/δ (Jiménez 2004). One consequence of this choice is that it is more likely that a sandpaper-type roughness (figure 2A) is matched with another study of a different sandpaper grit. Additionally, only cases in the fully rough regime ($\Delta U_I^+ \geq 7$) are considered. Whenever possible, the roughness geometry (i.e. the streamwise and spanwise spacing or the extent of the roughness elements, λ_x and λ_z illustrated in table 5) and some flow-related properties, Re_τ and ΔU_I^+ (for $M > 1$, ΔU^+ if $M \approx 0$), are also matched.

Table 5 lists the matched compressible and incompressible test cases. The incompressible equivalents are found for all roughness families in figure 2, except for the diamond-type roughness (figure 2G). For every matched roughness family, the closest matching δ/k case exists, except for the present P24 test cases. As there is no incompressible sandpaper test case that can match $\delta/k \approx 8.4$, a cube roughness (figure 2D) of Castro (2007) ($\delta/k \approx 9.6$) is chosen as the incompressible equivalent of the P24 test cases. While the majority of the previous studies in table 2 must be matched with other studies in the incompressible flow regime, for the sine wave roughness (figure 2C) of Tyson & Sandham (2013) and the cube roughness of Modesti *et al.* (2022), the incompressible equivalents are taken from the simulations of the same rough surfaces at $M_b = 0.3$. Since k_s is not reported by Tyson & Sandham (2013), it is derived from the reported ΔU^+ via equation (1.2). The reported k_s/k (table 5) of the incompressible test cases are then utilised to find the equivalent sand grain roughness k_{si} for the matched compressible test cases,

$$k_{si} = \left. \frac{k_s}{k} \right|_{M \approx 0} k|_{M > 1} \quad (4.1)$$

Figure 6(b) shows the reported ΔU_I^+ for the present and previous test cases as a function of $k_{si}^+ = k_{si} U_\tau / \nu_w$. Black solid line represents Nikuradse’s formula for rough walls in incompressible flow regime, while the hatched region is the $\pm 10\%$ deviation from the formulation. Coloured open and gray filled symbols are the data from current and previous compressible flow studies, respectively, with the symbols corresponding to various studies in table 2 and 3. For the current dataset, k_{si} obtained from the matched incompressible test cases (table 5) collapses ΔU_I^+ to Nikuradse’s data for P60 and P24 test cases at $M = 2$, for both lower and higher Re (table 3), although notably less so for the P24 test surface at the higher Re ($Re_\tau = 30292$, open purple symbols in figure 6b). On the other hand, k_{si} fails to collapse ΔU_I^+ for $M = 2.9$ test cases, suggesting that k_s , to an extent, is a function of M , which has also been suggested if k_s from the $M = 0.3$ data is instead utilised (figure 5e,f). However, the estimated k_{si} for the cube roughness of Modesti *et al.* (2022) collapses the reported ΔU_I^+ of the fully rough test cases, across the Mach number and Re sweeps ($M = 2$ and 4, $1034 \leq Re_\tau \leq 3659$), within $\pm 10\%$ error from Nikuradse’s formula. This suggests

the possibility of other criteria to consider for finding k_{si} beyond matching roughness type and δ/k .

First, we consider the roughness geometry as a possible additional criterion for k_{si} determination. For the 2D traverse bars (figure 2B) of Sahoo *et al.* (2009), whose $\lambda/k = 5$ is identical to those of Leonardi *et al.* (2003), the k_{si} obtained from the latter study collapses the ΔU_I^+ . However, k_{si} fails to collapse the ΔU_I^+ of a 2D sine waves of Tyson & Sandham (2013), although the roughness geometry was identical to that simulated at $M = 0.3$. And yet, k_{si} from the cube roughness of Castro (2007) predicts the drag of the same roughness type of Ekoto *et al.* (2008) relatively well, even though the roughness element spacing in the first study is less than half of the latter ($\lambda_x/\delta = \lambda_z/\delta = 0.11$ and 0.27 , respectively).

The second additional criterion to consider is matched Re . Data from previous studies seem to suggest that this is not a determining factor: the obtained k_{si} for the P24-grit sandpaper of Reda *et al.* (1975), as well as P36- and P20-grit sandpapers of Latin & Bowersox (2000), are able to collapse the ΔU_I^+ even though the Re_τ do not precisely match their incompressible equivalents. Latin & Bowersox (2000), for example, conducted the studies at $Re_\tau \approx 5000$, while Flack *et al.* (2007) at $Re_\tau \approx 4000$. A closer match of $Re_\tau \approx 3000$ between the sandpapers of Latin & Bowersox (2000) and Brzek *et al.* (2007), as well as the matched ΔU_I^+ of the cube roughness of Latin & Bowersox (2000) and ΔU^+ of Volino *et al.* (2011), on the other hand, fail to obtain an accurate k_{si} for the aforementioned test surfaces at compressible flow regime. Taken together, these observations from present and previous studies seem to suggest that there is no distinct criterion that can guarantee the success of using k_{si} from available incompressible flow data to predict the drag of rough walls in their equivalent compressible flow test cases – neither the roughness-related criteria (family type, physical height, and geometry) nor the flow-related criteria (Re_τ or ΔU^+). This leads to another possible correction factor of k (or k_s from incompressible flow data), by considering some compressibility effects within the flows.

4.2. Scaling based on T_∞/T_w

So far, ΔU_I^+ in figures 5(e,f) and 6(a,b) are presented as a function of viscous-scaled k or k_s . Here, the viscous lengthscale U_τ/ν_w is a quantity defined by flow properties at the wall, $U_\tau = \sqrt{\tau_w/\rho_w}$. Previous studies suggested that a better collapse to Nikuradse’s formula in incompressible flow regime was observed if flow properties at another wall-normal location related to the roughness were used to scale k or k_s instead of those at the wall. In the cube roughness (figure 2D) of Modesti *et al.* (2022), a correction factor based on the kinematic viscosity ratio $\nu_k^+ = \nu_k/\nu_w$ was introduced to the cube physical height, $k_*^+ = k/\nu_k^+$ (subscript ‘k’ denotes properties at the tip of the roughness elements), such that a collapse to Nikuradse’s formula is observed when ΔU_I^+ (for various transformations) was scaled by $k_{s*}^+ = 1.9kU_\tau/\nu_k$, with $k_s/k = 1.9$ is the k_s obtained from numerical simulations of the same roughness at $M = 0.3$. A similar scale of $k_*^+ = (k\sqrt{\tau_w/\rho_k})/\nu_k$ was utilised for the cube and 2D traverse bar roughness (figure 2B) of Neeb *et al.* (2016).

Unfortunately, these correction factors based on the properties at the tip of the roughness elements are not able to collapse ΔU_I^+ for the present test cases in table 3. What seems to suit these cases better is a correction factor based on the freestream, rather than the roughness tip, properties: $\nu_\infty^+ = \nu_\infty/\nu_w$, which is obtained from T_∞/T_w ratio via equation (2.4). Open symbols in figure 6(c) shows ΔU_I^+ of all test cases in table 3, with various transformations for compressibility effects (table 1) across M and Re_τ sweeps, collapses to Nikuradse’s formula (within $\pm 10\%$ error marked by the hatched region in the figure) when presented as a function of $k_*^+ = kU_\tau/\nu_\infty$.

We further examine this correction factor for the previous studies listed in table 2. Finding

the correction factor ν_∞^+ for these studies requires some knowledge regarding the freestream-to-wall temperature ratios T_∞/T_w (or bulk-to-wall temperature ratio T_b/T_w) and the viscosity models as a function of the temperature profiles. These quantities were not explicitly reported in the majority of studies in table 2. Therefore, the temperature ratios T_∞/T_w are calculated from either the temperature profiles (if reported) or from the isentropic relation (if T_0 , M_∞ , and T_w were reported). The dynamic viscosity ratio $\mu_\infty^+ = \mu_\infty/\mu_w$ is then estimated, typically as an exponential function of the temperature profile, $\mu^+ = (T/T_w)^\omega$, where ω is a constant. If the model used to calculate μ^+ was not reported in the study, Sutherland's model (equation 2.4), which is also used in present study, is assumed. For previous studies in the hypersonic flow regime, where the static temperature may reach below 100 K, unless the viscosity model was reported, Keyes's model is assumed (Keyes 1951; Roy & Blottner 2006). With these assumptions, the correction factors ν_∞^+ can be estimated for all previous studies, with the exception of the sandpaper roughness of Goddard (1959), the 2D sine wave of Tyson & Sandham (2013) and Aghaei-Jouybari *et al.* (2023), and the egg carton roughness (figure 2E) of Aghaei-Jouybari *et al.* (2023). Gray-filled symbols in figure 6(c) show the reported ΔU_I^+ as a function of $k_*^+ = kU_\tau/\nu_\infty$ for test cases in table 2 (where ν_∞^+ can be estimated). Unlike the present study, the ν_∞^+ correction factor does not collapse the majority of ΔU_I^+ of previous studies to Nikuradse's formula (within $\pm 10\%$ error from the formula, shown by hatched region in figure 6c), except for the P80-grit sandpaper of Latin & Bowersox (2000), test cases at $M_b = 2$ of Modesti *et al.* (2022), and a test case at $M_\infty = 2.25$ of Wang & Gao (2024).

Due to poor performance of the correction factor ν_∞^+ to scale the roughness physical height k in the x -axis of figure 6(c), we develop another correction factor for ΔU_I^+ (the y - instead of x -axis of figure 6c). Considering the relation between the skin friction coefficient C_f and ΔU^+ in equation (1.3), we introduce a new correction factor for ΔU_I^+ , $\sqrt{1/F_c}\Delta U_I^+$, where F_c is the correction factor for smooth-wall TBL skin friction, $F_c C_f$, derived from the VD II transformation van Driest (1956). For the present experimental data, F_c is calculated using equation (3.1) as a function of T_∞/T_w . Open symbols in figure 6(d) shows the corrected ΔU_I^+ as a function of k^+ for all test cases in table 3, of various transformations (table 1) across M and Re_τ sweeps. All test cases collapse to Nikuradse's formula (within $\pm 10\%$ error marked by the hatched region in the figure) when the correction factor $\sqrt{1/F_c}$ is applied to the experimental data.

In line with the previously tested correction factors, the $\sqrt{1/F_c}$ correction factor is tested for previous studies in table 2. Due to various wall conditions of the experiments and simulations (either adiabatic, isothermal, or a constant cooling rate is applied), a more general form of VD II transformation (van Driest 1956) was derived by Hopkins & Inouye (1971) to obtain the correction factor F_c

$$F_c = \frac{r^{\frac{\gamma-1}{2}} M_\infty^2}{(\arcsin \alpha + \arcsin \beta)^2} \quad (4.2)$$

where

$$\alpha = \frac{2A^2 - B}{\sqrt{4A^2 + B^2}} \quad \text{and} \quad \beta = \frac{B}{\sqrt{4A^2 + B^2}} \quad (4.3)$$

$$A = \sqrt{\frac{r^{\frac{\gamma-1}{2}} M_\infty^2}{T_w/T_\infty}} \quad \text{and} \quad B = \frac{1 + r^{\frac{\gamma-1}{2}} M_\infty^2 - T_w/T_\infty}{T_w/T_\infty} \quad (4.4)$$

The temperature ratio T_∞/T_w is obtained either from the temperature profiles or the isentropic relation, as described in the steps to obtain the previous correction factor ν_∞^+ . For studies

conducted on adiabatic walls (whether assumed or measured directly, as marked by **(b)** and **(c)** in table 2), equation (4.2) reduces to (3.1). Gray-filled symbols in figure 6(d) show the ΔU_I^+ corrected by $\sqrt{1/F_c}$ as a function of k^+ . In general, this correction factor performs better than scaling the x -axis by $k_* = k/\nu_\infty^+$, shown in figure 6(c), for collapsing ΔU_I^+ onto Nikuradse's formula. Within $\pm 10\%$ error of the formula (hatched region in figure 6d), the drag of the following test surfaces can be estimated: all sandpaper roughnesses of Reda *et al.* (1975) and two sandpaper grits (P36 and P20) of Latin & Bowersox (2000), a test case each of the 2D traverse bars of Berg (1979), Latin & Bowersox (2000), and Sahoo *et al.* (2009), the cube roughnesses of Latin & Bowersox (2000), as well as Modesti *et al.* (2022) for all $M_b = 2$ test cases and only the higher Re_τ cases at $M_b = 4$, the egg carton roughness of Wang & Gao (2024) at $M_\infty \leq 3.5$, and the mesh roughness of Sahoo *et al.* (2009).

5. Discussions

It is not clear at this point why some correction factors that collapse either ΔU_I^+ , k^+ , or k_s^+ into Nikuradse's formula perform better or worse than others. As shown in §4.1 and figure 6(b), when the roughness type and geometry (i.e. δ/k) are matched to an equivalent study in incompressible flow and the equivalent k_{si} is utilised, there is no clear indicator as to why an estimated k_{si} for a certain roughness can collapse ΔU_I^+ of a rough surface to Nikuradse's formula while another k_{si} for another roughness cannot. Adding flow conditions into consideration, in this case either Re_τ or ΔU^+ , does not yield clearer criteria for roughness matching that guarantee the success of the estimated k_{si} . This suggests that there are other factors at play, such as compressibility, that have not been considered by this method.

Some measures of compressibility are taken into account in §4.2. The first is a correction factor on the x -axis of ΔU_I^+ as a function of k_s^+ or k^+ . Typically, this involves some viscosity and/or density correction factor of k_s^+ or k^+ (where k_s is obtained from an equivalent incompressible test case) such that ΔU_I^+ (obtained from the transformed velocity profile) collapses onto Nikuradse's formula. Here, the density and viscosity profiles are obtained from the temperature profile, with an assumed viscosity model (see for example, equation 2.4). This approach has been documented in previous studies, such as Neeb *et al.* (2016) and Modesti *et al.* (2022) for cube and 2D traverse bar roughnesses (figures 2B and C), using density and/or kinematic viscosity at the tip of the roughness element, ρ_k and ν_k . To the best of our knowledge, these correction factors were empirical (i.e. not derived analytically) and have not been tested on other roughnesses in other studies. With the present experimental data (table 3), scaling k^+ with the *freestream-to-wall* air viscosity ratio $\nu_\infty^+ = \nu_\infty/\nu_w$, rather than the tip of the roughness element, collapses the data onto Nikuradse's formula in the fully rough regime (equation 1.2). The same scaling factor (using the freestream viscosity) has a very limited success when tested on data from previous studies (table 2) within transitionally and fully rough regimes, as shown in figure 6(c). Similar to the other correction factor, which uses air properties at the roughness tip, the freestream correction factor is also determined empirically.

A more promising correction factor is one on the y -axis, ΔU_I^+ multiplied by $\sqrt{1/F_c}$ (figure 6d), where F_c a function of freestream-to-wall temperature ratio, T_∞/T_w (equations 3.1 and 4.2). F_c is a correction factor derived from the van Driest (1956) II transformation for C_f of *smooth-wall* boundary layers. Using this correction factor, the present experimental data collapse onto Nikuradse's formula in the fully rough regime (table 3). When tested for the data from previous studies (table 2), the $\sqrt{1/F_c}$ has better success in collapsing the ΔU_I^+ compared to the other correction factors tested in the study (figure 6d): using the incompressible equivalent k_s (§4.1) and scaling k^+ (or k_s^+) by the freestream viscosity (§4.2). Notably,

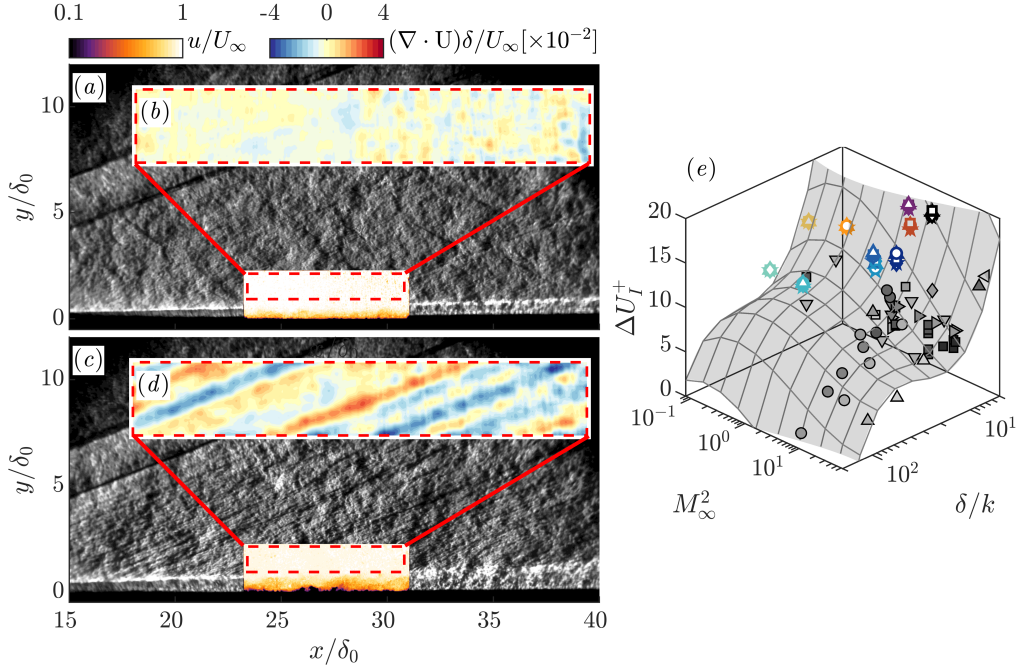


Figure 7: Instantaneous Schlieren image of test case (a) SW and (c) P24 at $M = 2.9$, overlaid by an instantaneous streamwise velocity u/U_∞ obtained from PIV measurements (not simultaneously acquired), where δ_0 is the reference boundary-layer thickness (case SW at $M = 0.3$, see also figure 3c). *Inset*: time-averaged velocity divergence $\nabla \cdot \mathbf{U}$ normalised by δ/U_∞ of the same (b) SW and (d) P24 test cases at the freestream, the area marked by red dashed lines in (a, c). (e) Surface of ΔU_T^+ as a function of $\log M_\infty^2$ (or M_b^2 for channel flow cases) and $\log(\delta/k)$, obtained from fitting the present experimental results (open coloured symbols in table 3) and data from previous studies (gray-filled symbols in table 2).

these studies outlined in table 2 span supersonic to hypersonic freestream (or bulk) velocities, Reynolds numbers, transitionally to fully rough regimes, and perhaps more crucially, various techniques to obtain the wall-shear stresses (whether through direct measurements or fitting methods, as is the case with present experimental data), as well as various wall conditions (direct T_w measurements, assumed T_w , or wall treatments, e.g. cooled with a constant cooling rate). However, similar to the previous correction factors for k^+ or k_s^+ involving some density or viscosity of the flow, either at the tip of the roughness or in the freestream, this correction factor is, too, empirical. In fact, the Hama roughness function ΔU_T^+ is obtained by vertically shifting a transformed velocity profile (table 1 and §2.5), and thus multiplying this quantity by $\sqrt{1/F_c}$ is, in a sense, performing the transformation twice.

Perhaps, the flow fields should be re-examined. Figure 7(a) shows an instantaneous Schlieren image in the x - y plane of the SW test case at $M = 2.9$, taken by a pco.Dimax S4 high-speed camera and overlaid by an instantaneous u/U_∞ flow field obtained from the 2D2C PIV measurements at the same plane (not simultaneously acquired). The leading-edge oblique shockwave is captured by the Schlieren image, visible on the left-hand side of figure 7(a). Inset (b) of the same figure captures the time-averaged velocity divergence $\nabla \cdot \mathbf{U} = \partial U/\partial x + \partial V/\partial y$ at the freestream (red dashed lines in figure 7a), obtained from PIV measurements and normalised by δ/U_∞ . For the SW test case, the divergence at the freestream approaches zero, as shown in figure 7(b). By contrast, the instantaneous Schlieren

image of the P24 test case at the same nominal $M = 2.9$ (figure 7c) reveals a succession of shockwaves (or more accurately, bow shocks) in front of the roughness elements in the streamwise direction, which is related to the additional wave drag in compressible flows. Furthermore, these waves are persistent and extend well into the freestream: they are also observed in the time-averaged flow field, as shown by the mean velocity divergence in the freestream (figure 7d). The current framework for drag characterisation in compressible, rough-wall TBLs (figure 1) does not account for the additional wave drag inferred from figure 7(c,d), as the velocity profiles are stretched with transformations developed or derived from *smooth*-wall, rather than *rough*-wall, TBLs (examples of such transformations are outlined in table 1). In the future, a custom transformation for a rough-wall TBL, which accounts for the properties of a particular roughness, should be considered.

Ultimately, drag characterisation in compressible, rough-wall TBLs aims to build a “map” of a drag quantity (either C_f or ΔU_I^+ , as shown in figure 7e) as a function of roughness properties (or a custom compressibility transformation for a rough wall), inflow Mach number M_∞ (or M_b for channel flow cases), and possibly other factors (e.g. wall conditions). Data from previous studies, both experimental and computational (listed in table 2), are unfortunately limited. And while the present experimental data bridge the data gap in the high Re regime, with independent sweeps of M and Re spanning the subsonic, transonic, and supersonic flow regimes, direct measurements of wall-shear stress, wall temperatures, and temperature profiles are not carried out due to limitations of the experimental facility. These measurements should be carried out in future studies to ensure an accurate drag characterisation. However, measuring properties at the wall, or, as suggested by some studies, at the tip of the roughness, is non-trivial. This is especially true for non-homogeneous, irregularly-shaped roughness, akin to the sandpaper roughness tested in this study, which is more likely to arise from impact and ablation during the operation of a high-speed vehicle.

6. Conclusions and future work

Experiments are carried out for TBLs developing over two types of sandpaper rough walls (P60- and P24-grit) in order to establish a framework for drag characterisation in compressible TBLs using the existing framework (Nikuradse 1933; Hama 1954) and information for the same rough surfaces in incompressible TBLs (figure 1). The test cases span both incompressible and compressible flow regimes ($0.3 \leq M \leq 2.9$) and $7427 \leq Re_\tau \leq 30292$, with an independent variation of Re_τ at a constant $M = 2$. Due to the limitations of the test facility, the wall-shear stress is estimated using a fitting method outlined in §2.5 and an adiabatic wall is assumed (§2.5).

Present results suggest that all test cases in table 3 fall into the fully rough regime and that the Hama roughness function (or the momentum deficit) ΔU_I^+ in the compressible flow regime is relatively independent of the velocity transformations to account for the compressibility effect (table 1, figure 6a). The log-law intercept of $B - B_{FR}$ (equation 1.2), however, seems to increase proportionally with M . This is not taken into account in the existing log relation in the fully rough regime (equation 1.2) for incompressible flow. Therefore, to be able to utilise the existing framework for drag characterisation, either the roughness lengthscale k^+ or k_s^+ or the ΔU_I^+ must be scaled by a factor.

Three scaling factors are introduced and tested for the present experimental data and the available data from previous studies described in table 2 involving various roughness types illustrated in figure 2. The first is an equivalent k_s obtained from a similar incompressible flow study (the same roughness type and comparable roughness length-scale δ/k), followed by a correction factor in k , $k_* = k/\nu_\infty^+$, and finally a correction factor for C_f in the momentum

deficit ΔU_I^+ , $\sqrt{1/F_c}\Delta U_I^+$, where F_c is a function of T_∞/T_w (equations 3.1 and 4.2). When tested for the current and previous compressible flow data, the first method has limited success (figure 6b). Both second and third methods collapse the present experimental data into the log relation (figures 6c,d). The latter shows more promising results when tested for data from previous studies (figure 6d).

However, it should be noted that all correction factors tested in this study are obtained empirically and that the drag and wall temperature are not directly measured. Furthermore, the current drag characterisation framework (Figure 1) uses compressibility transformations derived for smooth-wall TBLs (table 1) and the proposed correction factor F_c , which shows the most promising result, was originally derived for the correction of the smooth-wall C_f . In the future, direct wall-shear stress and wall temperature measurements should be conducted to ensure an accurate drag characterisation. Using these data, a custom transformation for a rough-wall TBL should be developed, which accounts for the properties of a particular roughness, the wave drag formed by the shock generated by the roughness elements, and the wall conditions.

Funding. The study is funded by the German Research Foundation (DFG, grant no. 448354709). DDW acknowledges funding from the Leverhulme Early Career Fellowship (grant no. ECF-2022-295). BG acknowledges funding from EPSRC (Grant Ref: EP/W026090/1).

Declaration of interests. The authors report no conflict of interest.

Data availability statement. The data that support the findings of this study will be made available upon publication at the University of Southampton's repository.

Author ORCIDs.

D. D. Wangsawijaya, <https://orcid.org/0000-0002-7072-4245>;

R. Baidya, <https://orcid.org/0000-0002-6148-602X>;

S. Scharnowski, <https://orcid.org/0000-0002-6452-2954>;

B. Ganapathisubramani, <https://orcid.org/0000-0001-9817-0486>;

C. J. Kähler, <https://orcid.org/0000-0001-9336-2091>.

REFERENCES

- ADRIAN, R. J. & WESTERWEEL, J. 2011 *Particle Image Velocimetry*, 1st edn. *Cambridge Aerospace Series*. New York: Cambridge University Press.
- AGHAEI-JOUYBARI, M., YUAN, J., LI, Z., BRERETON, G. J. & JABERI, F. A. 2023 Supersonic turbulent flows over sinusoidal rough walls. *J. Fluid Mech.* **956**, A3.
- BAIDYA, R., SCHARNOWSKI, S., BROSS, M. & KÄHLER, C. J. 2020 Interactions between a shock and turbulent features in a Mach 2 compressible boundary layer. *J. Fluid Mech.* **893**, A15.
- BERG, D. E. 1979 Surface roughness effects on a Mach 6 turbulent boundary layer. *AIAA J.* **17** (9), 929–930.
- BRUN, C., BOIARCIUC, M. P., HABERKORN, M. & COMTE, P. 2008 Large eddy simulation of compressible channel flow: Arguments in favour of universality of compressible turbulent wall bounded flows. *Theor. Comput. Fluid Dyn.* **22**, 189–212.
- BRZEK, B., CAL, R. B., JOHANSSON, G. & CASTILLO, L. 2007 Inner and outer scalings in rough surface zero pressure gradient turbulent boundary layers. *Phys. Fluids* **19**, 065101.
- CASTRO, I. P. 2007 Rough-wall boundary layers: mean flow universality. *J. Fluid Mech.* **585**, 469–485.
- CHAN, L., MACDONALD, M., CHUNG, D., HUTCHINS, N. & OOI, A. 2015 A systematic investigation of roughness height and wavelength in turbulent pipe flow in the transitionally rough regime. *J. Fluid Mech.* **771**, 743–777.
- CLAUSER, F. H. 1954 Turbulent boundary layers in adverse pressure gradients. *J. Aero. Sci.* **21** (2), 91–108.
- CROCCO, L. 1948 The laminar boundary layer in gases. *Tech. Rep.*. North American Aviation, Aerophysics Laboratory.
- EKOTO, I. W., BOWERSOX, R. D. W., BEUTNER, T. & GOSS, L. 2008 Supersonic boundary layers with periodic surface roughness. *AIAA J.* **46** (2), 487–497.
- FLACK, K. A., SCHULTZ, M. P. & CONNELLY, J. S. 2007 Examination of a critical roughness height for outer layer similarity. *Phys. Fluids* **19**, 095104.

- GODDARD, F. E. 1959 Effect of uniformly distributed roughness on turbulent skin-friction drag at supersonic speeds. *J. Aerosp. Sci.* **26** (1), 1–15.
- GUL, M. & GANAPATHISUBRAMANI, B. 2021 Revisiting rough-wall turbulent boundary layers over sand-grain roughness. *J. Fluid Mech.* **911**, A26.
- HAMA, F. R. 1954 Boundary layer characteristics for smooth and rough surfaces. *Trans. Soc. Nav. Arch. Marine Engrs.* **62**, 333–351.
- HOPKINS, E. J. & INOUE, M. 1971 An evaluation of theories for predicting turbulent skin friction and heat transfer on flat plates at supersonic and hypersonic Mach numbers. *AIAA J.* **9** (6), 993–1003.
- HOWARTH, L. 1948 Concerning the effect of compressibility on laminar boundary layers and their separation. *Proc. R. Soc. London, Ser. A* **194** (1036), 16–42.
- HUDSON, J. D., DYKHNO, L. & HANRATTY, T. J. 1996 Turbulence production in flow over a wavy wall. *Exp. Fluids* **20**, 257–265.
- JIMÉNEZ, J. 2004 Turbulent flows over rough walls. *Annu. Rev. Fluid Mech.* **36** (1), 173–196.
- KÄHLER, C. J., SAMMLER, B. & KOMPENHANS, J. 2002 Generation and control of tracer particles for optical flow investigations in air. *Exp. Fluids* **33**, 736–742.
- KEYES, F. G. 1951 A summary of viscosity and heat-conduction data for He, A, H₂, O₂, N₂, CO, CO₂, H₂O, and air. *Trans. ASME* **73** (5), 589–595.
- KROGSTAD, P.-Å., ANDERSSON, H. I., BAKKEN, O. M. & ASHRAFIAN, A. 2005 An experimental and numerical study of channel flow with rough walls. *J. Fluid Mech.* **530**, 327–352.
- LATIN, R. M. & BOWERSOX, R. D. W. 2000 Flow properties of a supersonic turbulent boundary layer with wall roughness. *AIAA J.* **38** (10), 1804–1821.
- LAWSON, J. M. 2016 A scanning PIV study of homogeneous turbulence at the dissipation scale. PhD thesis, University of Cambridge, code repository at <https://git.soton.ac.uk/jml1g18/pivtools>.
- LEONARDI, S., ORLANDI, P., SMALLEY, J., DJENIDI, L. & ANTONIA, R. A. 2003 Direct numerical simulations of turbulent channel flow with transverse square bars on one wall. *J. Fluid Mech.* **491**, 229–238.
- MODESTI, D., SATHYANARAYANA, S., SALVADORE, F. & BERNARDINI, M. 2022 Direct numerical simulation of supersonic turbulent flows over rough surfaces. *J. Fluid Mech.* **942**, A44.
- NEEB, D., GÜLHAN, A. & MERRIFIELD, J. A. 2016 Rough-wall heat flux augmentation analysis within the ExoMars project. *J. Spacecr. Rockets* **53** (1), 121–133.
- NEEB, D., MARQUARDT, P. & GÜLHAN, A. 2024 Characterization of a hypersonic turbulent boundary layer along a sharp cone with smooth and transverse square-bar roughened wall. *Exp. Fluids* **65**, 144.
- NIKURADSE, J. 1933 Laws of flow in rough pipes. *NACA Tech. Mem.* **1292**.
- PELTIER, S. J., HUMBLE, R. A. & BOWERSOX, R. D. W. 2016 Crosshatch roughness distortions on a hypersonic turbulent boundary layer. *Phys. Fluids* **28**, 045105.
- PIROZZOLI, S. & BERNARDINI, M. 2011 Turbulence in supersonic boundary layers at moderate Reynolds number. *J. Fluid Mech.* **688**, 120–168.
- REDA, D. C., KETTER, F. C. & FAN, C. 1975 Compressible turbulent skin friction on rough and rough/wavy walls. *AIAA J.* **13** (5), 553–554.
- ROY, C. J. & BLOTTNER, F. G. 2006 Review and assessment of turbulence models for hypersonic flows. *Prog. Aerosp. Sci.* **42** (7-8), 469–530.
- SAHOO, D., SCHULTZE, M. & SMITS, A. 2009 Effects of roughness on a turbulent boundary layer in hypersonic flow. In *Proceedings of the 39th AIAA Fluid Dynamics Conference*, pp. AIAA 2009–3678. American Institute of Aeronautics and Astronautics.
- SCHARNOWSKI, S., BROSS, M. & KÄHLER, C. J. 2019 Accurate turbulence level estimations using piv/ptv. *Exp. Fluids* **60**, 1.
- SCHLICHTING, H. & GERSTEN, K. 1960 *Boundary-Layer Theory*, 4th edn. New York: McGraw-Hill.
- SQUIRE, D. T., MORRILL-WINTER, C., HUTCHINS, N., SCHULTZ, M. P., KLEWICKI, J. C. & MARUSIC, I. 2016 Comparison of turbulent boundary layers over smooth and rough surfaces up to high Reynolds numbers. *J. Fluid Mech.* **795**, 210–240.
- TRETTEL, A. & LARSSON, J. 2016 Mean velocity scaling for compressible wall turbulence with heat transfer. *Phys. Fluids* **28**, 026102.
- TYSON, C. J. & SANDHAM, N. D. 2013 Numerical simulation of fully-developed compressible flows over wavy surfaces. *Int. J. Heat Fluid Flow* **41**, 2–15.
- VAN DRIEST, E. R. 1951 Turbulent boundary layer in compressible fluids. *J. Aeronaut. Sci.* **18**, 1012.
- VAN DRIEST, E. R. 1956 The problem of aerodynamic heating. *Aeronaut. Engng. Rev.* **15** (10), 26–41.

- VOLINO, R. J., SCHULTZ, M. P. & FLACK, K. A. 2011 Turbulence structure in boundary layers over periodic two- and three-dimensional roughness. *J. Fluid Mech.* **676**, 172–190.
- VOLPIANI, P. S., IYER, P. S., PIROZZOLI, S. & LARSSON, J. 2020 Data-driven compressibility transformation for turbulent wall layers. *Phys. Rev. Fluids* **5**, 052602(R).
- WALZ, A. 1959 Compressible turbulent boundary layers with heat transfer and pressure gradient in flow direction. *J. Research Natl. Bur. Standards* **63**.
- WANG, Y. & GAO, Z. 2024 Roughness effects on compressible turbulent boundary layers under different Mach numbers and wall temperature conditions. *Phys. Fluids* **36**, 025144.